Advanced Materials & Sustainable Manufacturing

Article

Cooling Channel Design and Temperature Field Analysis of a Lightweight High-Efficiency Drive Motor

Gang Lv *, Cheng-Yuan Ren, Zhong-Liang Liu, Wang Yu and Zhi-Le Chen

School of Electrical Engineering, Beijing Jiaotong University, Beijing 100044, China; 24110420@bjtu.edu.cn (C.-Y.R.); 23126323@bjtu.edu.cn (Z.-L.L.); 21117004@bjtu.edu.cn (W.Y.); 25110521@bjtu.edu.cn (Z.-L.C.)

* Corresponding author. E-mail: ganglv@bjtu.edu.cn (G.L.)

Received: 17 July 2026; Revised: 3 September 2026; Accepted: 17 September 2026; Available online: 21 September 2026

ABSTRACT: The temperature rise in lightweight, high-efficiency traction motors for new energy vehicles (NEVs) directly affects their operating efficiency, reliability, and service life. In this study, a permanent magnet synchronous motor (PMSM) for NEVs was selected as the research object, and three distributed cooling channel configurations, namely spiral, tree-shaped, and circumferential channels, were comparatively investigated using conjugate fluid–thermal simulations. The effects of cooling-channel configuration and coolant flow rate on the motor temperature and flow characteristics were analyzed. Under the rated operating condition with a total coolant flow rate of 10 L/min, the maximum motor temperatures of the spiral, tree-shaped, and circumferential configurations were 98.2 °C, 97.2 °C, and 99.6 °C, respectively. The tree-shaped cooling channel, therefore, exhibited the best thermal performance and the smallest maximum inlet-to-outlet static gauge-pressure difference among the three configurations. Based on the thermal constraints and the variation in this defined pressure metric, recommended coolant flow rates of 12 L/min and 22 L/min were selected for the peak-speed and peak-torque operating conditions, respectively.

Keywords: New energy vehicle; Permanent magnet synchronous motor; Cooling channel; Conjugate heat transfer

1. Introduction

The high efficiency and low power loss of traction motors are critical to improving the safety, dynamic performance, and driving range of new energy vehicles (NEVs), and have become a major research focus in the field of electric drive systems [1]. Owing to their high power density, high power factor, high starting torque, and low acoustic noise, permanent magnet synchronous motors (PMSMs) have been widely employed in NEV propulsion systems. However, the continuous increase in power density has led to a significant rise in the internal thermal load of the motor. Excessive temperature rise may result in irreversible demagnetization of permanent magnets and thermal deformation of motor components, thereby degrading electromagnetic performance, shortening the service life of the motor, and ultimately threatening its safe and reliable operation [2–4]. Therefore, accurate prediction of motor temperature rise and rational design of the cooling system are essential for improving the safety, reliability, and overall performance of NEV traction motors.

The temperature rise of traction motors is commonly predicted using simplified analytical methods, equivalent thermal network (ETN) methods, and numerical simulation methods [5]. Simplified analytical methods transform complex three-dimensional heat transfer problems into solvable algebraic models through a series of simplifying assumptions. Although these methods offer high computational efficiency, they generally cannot accurately capture the actual temperature distribution within the motor. In contrast, the ETN method is based on the field-circuit coupling principle, in which the distributed thermal system is represented by a lumped-parameter thermal network consisting of thermal resistances and thermal capacitances. This approach provides a favorable balance between computational efficiency and prediction accuracy.

In recent years, extensive studies have been conducted on motor thermal analysis based on the ETN method. Wang and Lin [6] proposed an electromagnetic–thermal bidirectional coupling method for the temperature field analysis of an interior permanent magnet synchronous motor (IPMSM). The model considered temperature-dependent material properties and various motor losses, and its accuracy was verified experimentally, with the temperature prediction error controlled within 4%. Boglietti et al. [7] established a thermal network model for a self-ventilated variable-speed induction motor, and experimental results verified the effectiveness of the proposed method. Lim CH et al. [8] developed an equivalent thermal circuit model for the steady-state thermal analysis of an axial-flux generator, demonstrating its capability to accurately predict the surface temperature distribution. Ghahfarokhi P. S. et al. [9] proposed an ETN model for synchronous reluctance motors, and experimental validation confirmed its effectiveness in temperature field prediction.

Numerical simulation methods, including the finite difference method (FDM) and finite element method (FEM), have become widely adopted for motor thermal analysis because of their high prediction accuracy and ability to resolve both global and local temperature distributions. Wahsh et al. [10] established a three-dimensional thermal model of an axial-flux PMSM using the FEM and investigated the influence of rotational speed on the steady-state temperature distribution under full-load conditions. Zhou et al. [11] proposed a hybrid subdomain and finite-difference method for rapidly predicting the magnetic and temperature fields of an interior permanent magnet synchronous motor. The calculated temperature-field results were validated through finite-element analysis and experimental testing. Joo D. et al. [12] proposed a three-dimensional magneto-thermal coupled simulation method based on the FEM for transient thermal analysis. Experimental results showed that the proposed method accurately predicts the motor's temperature evolution during continuous operation.

Water cooling has become the dominant thermal management solution for traction motors in new energy vehicles (NEVs) because of its high heat dissipation capability, compact structure, and low operating noise. In this cooling strategy, enclosed cooling channels are integrated into the motor housing, and heat generated during motor operation is removed by circulating coolant through the channels. In recent years, considerable efforts have been devoted to optimizing cooling channel configurations to improve the thermal performance of traction motors. Zhang K. et al. [13] designed three cooling channel configurations and employed a coupled electromagnetic–thermal–fluid multiphysics approach to evaluate their cooling performance. The optimal cooling structure was determined by comparing the maximum motor temperature achieved with each configuration. Ma Zhichao et al. [14] proposed a novel cooling channel design that effectively reduced the maximum temperature at the winding end region. Wang Yuyong et al. [15] developed a double-helical cooling channel and demonstrated that it provided superior heat dissipation performance compared with the conventional single-channel configuration. Wang Xiaofei et al. [16] investigated the effects of different operating conditions and coolant flow rates on motor temperature rise using a fluid–solid coupled analysis. Liu Chengbao et al. [17] proposed an improved multi-objective nonlinear magneto-thermal coupled iterative method with enhanced prediction accuracy and employed an orthogonal experimental design to investigate the effects of channel number, coolant inlet flow rate, cooling medium, and inlet/outlet channel arrangement on the thermo-fluid characteristics of the motor. Recent studies have further combined numerical thermal modeling with experimental validation and cooling-system optimization for traction motors. Tang et al. [18] established both lumped-parameter thermal network and three-dimensional CFD models for a 200-kW water-cooled permanent-magnet synchronous machine and experimentally validated the predicted temperature distributions under different operating conditions. K. Jeon et al. [19] employed electromagnetic–thermal–fluid coupled analysis and a design-of-experiments approach to investigate the effects of water-jacket configuration, coolant mass flow rate, and inlet/outlet arrangement on the cooling performance of a PMSM. Zhang et al. [20] investigated the coupled effects of channel number and coolant flow rate on the thermal and hydraulic characteristics of a liquid-cooled PMSM and proposed a Reynolds-number-based optimization strategy. More recently, Zhang et al. [21] combined three-dimensional CFD, thermal-network modeling, and experimental tests to evaluate a compound water-cooling system for an electric-vehicle PMSM. These studies demonstrate that both the cooling-channel geometry and the coolant-flow allocation have significant influences on the thermal and hydraulic performance of high-power-density traction motors.

Although substantial progress has been made in motor thermal modeling and cooling-system design, the studies summarized above mainly focus on thermal prediction methods, optimization of individual cooling-channel structures, or the influence of coolant flow rate. A systematic comparison of different practical cooling-channel configurations within the same traction-motor platform, while simultaneously considering thermal performance, coolant-flow, and static-pressure characteristics, structural material usage, and manufacturability, remains insufficiently addressed. In addition, the coolant flow rate required for different high-load operating conditions should be matched according to the corresponding thermal demands rather than using a single fixed flow rate for all operating conditions.

To address these issues, a permanent magnet synchronous traction motor for new energy vehicles (NEVs) is selected as the research object in this study. Three distributed cooling-channel configurations, namely spiral, tree-shaped, and circumferential channels, are designed and comparatively investigated. The originality and contributions of this work are mainly reflected in the following aspects: (1) the three cooling-channel configurations are evaluated under the same total coolant flow rate to provide a consistent comparison of their thermal and flow characteristics; (2) the evaluation considers motor temperature, coolant-flow distribution, maximum inlet-to-outlet static gauge-pressure difference, estimated channel volume, equivalent displaced aluminum mass, and manufacturing considerations; and (3) after identifying the preferred cooling-channel configuration, coolant-flow-rate matching is conducted under peak-speed and peak-torque operating conditions based on the temperature constraints and the variation in the defined static-pressure-difference metric. Through this integrated thermal and coolant-flow analysis, the present study provides a practical basis for cooling-system design and thermal management of lightweight NEV traction motors.

2. Theoretical Background

The water-cooling process of the traction motor involves coolant flow through the cooling channels, heat conduction within the solid motor components, and heat exchange between the solid regions and the coolant. In this study, a fluid–thermal coupled method is employed to numerically analyze the motor temperature field and the coolant flow field within the cooling channels. Based on the assumptions adopted in the subsequent numerical model, the coolant is treated as an incompressible fluid, while the effects of gravity and thermal radiation are neglected. Heat transfer is primarily considered in terms of thermal conduction among the motor components and convective heat transfer between the coolant and the cooling-channel walls. Accordingly, the coolant flow and heat transfer processes within the motor are mainly governed by the mass conservation equation, momentum conservation equation, energy conservation equation, and heat conduction equation in the solid regions [22–24].

For the incompressible coolant, the mass conservation equation can be expressed as [22,23]:

$$\frac{\partial \rho}{\partial t}+\frac{\partial(\rho v_x)}{\partial x}+\frac{\partial(\rho v_y)}{\partial y}+\frac{\partial(\rho v_z)}{\partial z}=0 \tag{1}$$

where ρ is the fluid density, t is the time, and v_x, v_y, v_z are the velocity components in the x-, y-, and z-directions, respectively.

The coolant flow through the cooling channels satisfies the law of conservation of momentum, and the corresponding governing equations can be expressed as [22,23]:

$$\begin{aligned}
\frac{\partial(\rho v_x)}{\partial t}+div(\rho v_x\overrightarrow{v_x})&=-\frac{\partial p}{\partial x}+div(\mu gradv_x)+S_{v_x}\\
\frac{\partial(\rho v_y)}{\partial t}+div(\rho v_y\overrightarrow{v_y})&=-\frac{\partial p}{\partial y}+div(\mu gradv_y)+S_{v_y}\\
\frac{\partial(\rho v_z)}{\partial t}+div(\rho v_z\overrightarrow{v_z})&=-\frac{\partial p}{\partial z}+div(\mu gradv_z)+S_{v_z}
\end{aligned} \tag{2}$$

where p is the pressure, μ is the dynamic viscosity, S_{vx}, S_{vy}, S_{vz} are the generalized source terms in the x-, y-, and z-directions. Equation (2) describes the velocity and pressure distributions of the coolant in different cooling channel configurations, providing the theoretical basis for the subsequent analysis of coolant velocity, static gauge-pressure distributions, and the defined maximum inlet-to-outlet static gauge-pressure difference.

The coolant flow process is accompanied by energy transfer, and the energy conservation equation can be expressed as [22,23]:

$$\frac{\partial(\rho T)}{\partial t}+div(\rho\vec{u}T)=div\left(\frac{\lambda}{C_p}gradT\right)+S_T \tag{3}$$

where C_p is the specific heat capacity at constant pressure, T is the temperature, λ is the thermal conductivity, S_T is the viscous dissipation term, and u is the fluid velocity.

For solid regions, including the stator, windings, rotor, permanent magnets, and motor housing, the temperature field is primarily governed by internal heat conduction and heat sources from motor losses. The corresponding heat conduction equation can be expressed as [22,24]:

$$\rho_s C_{p,s}\frac{\partial T}{\partial t}=div(\lambda_s gradT)+q_v \tag{4}$$

where ρ_s is the density of the solid material; $C_{p,s}$ is the specific heat capacity of the solid material; T is the temperature; λ_s is the thermal conductivity of the solid material; and q_v is the volumetric heat generation rate in the solid region, which is calculated from the power loss and the corresponding volume of each motor component.

Compared with simplified analytical and equivalent thermal network methods, the fluid-thermal coupled finite-element approach adopted in this study can directly represent the detailed geometries of the motor and cooling channels and resolve the spatial temperature distribution of individual components. This capability is particularly useful for identifying local hot spots and evaluating cooling-channel configurations with different flow-path arrangements. Moreover, the method simultaneously provides the temperature field of the solid components and the coolant velocity and static gauge-pressure fields, allowing the thermal, flow-distribution, and static-pressure characteristics to be examined within the same numerical framework. By incorporating electromagnetic loss data as volumetric heat sources and performing simulations over different operating conditions and coolant flow rates, the adopted approach also enables operating-condition-dependent coolant-flow matching. Therefore, this method is well suited to the comparative thermal and coolant-flow evaluation considered in the present study.

3. Motor Loss Calculation

The model of the double-V interior permanent magnet synchronous motor (IPMSM) for new energy vehicles investigated in this study is shown in Figure 1. The main geometrical and rated technical specifications used to establish the electromagnetic and thermal models are summarized in Table 1.

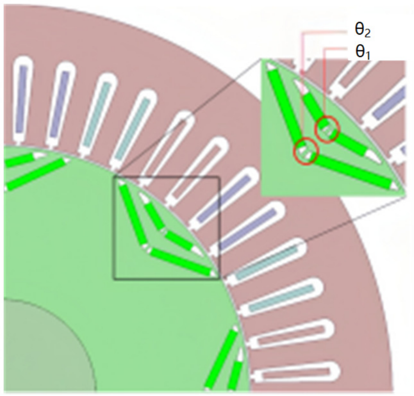

Figure 1. Quarter model of the double-V interior permanent magnet synchronous motor (IPMSM).

Table 1. Main parameters of the double-V interior permanent magnet synchronous motor (IPMSM).

Parameter	Value	Parameter	Value
Stator outer diameter (mm)	300	Rated power (kW)	85
Stator inner diameter (mm)	192	Rated speed (r/min)	3000
Rotor inner diameter (mm)	72	Rated torque (N·m)	270
Air gap length (mm)	1	Number of slots	48
Lamination stacking factor	0.95	Number of poles	8
V-angle 1	145°	V-angle 2	140°

The heat sources responsible for the motor temperature rise originate from the various power losses generated during motor operation [25]. The total power loss can be expressed as:

$$P_{\Sigma} = P_{\mathrm{c}} + P_{\mathrm{t1}} + P_{\mathrm{t2}} + P_{\mathrm{w}} + P_{\Delta} \tag{5}$$

where P_{Σ} is the total power loss, P_{c} is the stator winding copper loss, P_{t1} is the rotor iron loss, P_{t2} is the stator iron loss, P_{w} is the permanent magnet eddy current loss, and $P_{\triangle}$ is the sum of the mechanical loss and stray loss, which is calculated using an empirical formula.

The volumetric heat generation rate is used to characterize the amount of heat generated per unit volume per unit time due to power losses within the motor components. It serves as the heat source input for the thermal analysis and is expressed as [22]:

$$q = \frac{P}{V} \tag{6}$$

where q is the volumetric heat generation rate of the corresponding motor component, P is the corresponding power loss, and V is the volume of the corresponding component.

Motor losses were calculated using transient electromagnetic finite element analysis under rated, peak-speed, and peak-torque conditions. The stator iron loss, rotor iron loss, permanent-magnet eddy-current loss, and winding copper loss were obtained from the electromagnetic simulation results, and the corresponding volumetric heat generation rates were subsequently determined. The calculated power losses and corresponding volumetric heat generation rates under different operating conditions are listed in Table 2.

Table 2. Power losses and volumetric heat generation rates of motor components under different operating conditions.

Working Conditions	Power Losses (W)				Heat Generation Rates (W/m^3)			
	Stator Iron Loss	Rotor Iron Loss	PM Eddy Current Loss	Winding Copper Loss	Stator	Rotor	PMs	Windings
Rated	1422.6	26.76	5.88	1486.8	250,847.34	18,571.43	24,156.25	217,054.34
Peak speed	2123.1	196.2	40.74	1799	362,338.98	46,657.14	127,312.5	2,632,984.77
Peak torque	1653.8	31.3	6.42	2709.4	280,305.1	7452.4	20,062.5	3,816,056.34

4. Cooling Channel Design and Multiphysics Analysis of the Traction Motor

4.1. Water Jacket Design

The traction motor adopts a water-cooling system in which the cooling channels are integrated into the motor housing. Heat generated during motor operation is removed by the circulating coolant flowing through the cooling channels, thereby preventing excessive temperature rise caused by heat accumulation. The design of the cooling channels plays a crucial role in the cooling performance, operational reliability, and service life of the motor [26,27]. Therefore, the cooling channel configuration should ensure uniform cooling, sufficient heat dissipation capability, appropriate coolant flow velocity, and satisfactory manufacturability.

To investigate the effects of different cooling channel configurations on the thermal performance of the motor and the coolant flow characteristics, three cooling channel configurations, namely, spiral, tree-shaped, and circumferential configurations, were designed and comparatively analyzed. The corresponding models are shown in Figure 2, and their main structural parameters are listed in Table 3.

It should be noted that the three cooling channel configurations are not geometrically identical; their cross-sectional dimensions, channel volumes, and total heat-transfer areas differ, as summarized in Table 3. Therefore, the present comparison evaluates the thermal, coolant-flow, and static-pressure characteristics of three practical cooling-channel designs rather than isolating the effect of flow-path topology alone. In particular, although the tree-shaped and circumferential channels have the same cross-sectional area and perimeter, the circumferential channel has a larger channel volume and heat-transfer area. Thus, the subsequent thermal and flow-field results should be interpreted by considering the combined effects of channel geometry, coolant distribution, and flow-path arrangement.

From the perspective of lightweight design, the coolant-channel volume also affects the amount of aluminum material remaining in the water jacket. Since the three configurations use the same aluminum housing material and the same external housing envelope, a larger internal channel volume corresponds to a lower amount of remaining housing material. Based on the aluminum density of 2719 kg/m^3, the estimated channel volumes are equivalent to approximately 1.94, 2.24, and 2.43 kg of displaced aluminum for the spiral, tree-shaped, and circumferential configurations, respectively. Compared with the spiral configuration, the tree-shaped and circumferential configurations therefore correspond to approximately 0.30 and 0.48 kg less housing material, respectively. Because the original solid CAD models are no longer available, these values are used only as relative lightweight indicators rather than as absolute water-jacket masses.

Manufacturing feasibility should also be considered in practical applications. The spiral channel requires a long, continuous, curved flow path, whereas the tree-shaped configuration contains multiple branches and junctions, thereby involving greater machining and sealing complexity. The circumferential configuration has a relatively regular geometry, but suitable manifold connections are required to connect the individual circumferential passages. Therefore, manufacturing complexity should be considered together with thermal performance and material usage when selecting the cooling-channel configuration.

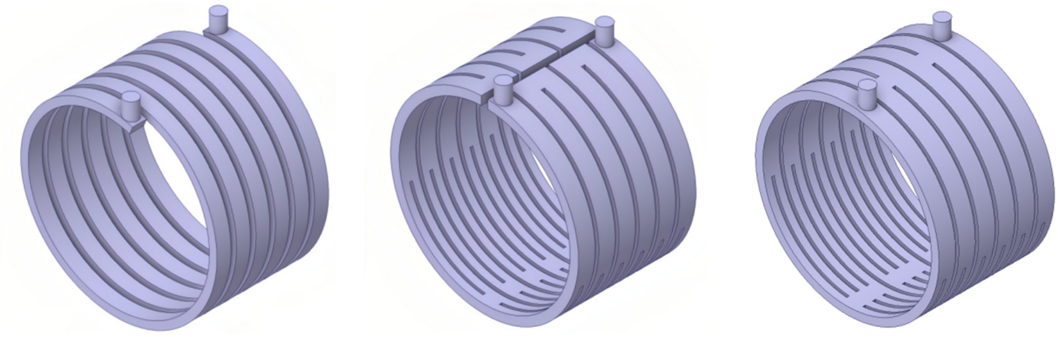

Figure 2. Three cooling channel configurations. (**a**) Spiral; (**b**) Tree-shaped; (**c**) Circumferential.

Table 3. Structural parameters of the three cooling channel configurations.

Parameter	Spiral	Tree-Shaped	Circumferential
Inlet/outlet diameter (mm)	25	25	25
Channel height (mm)	14	14	14
Channel width (mm)	26	31	31
Cross-sectional perimeter (mm)	80	90	90
Cross-sectional area (mm^2)	364	434	434
Total heat transfer area (m^2)	0.157	0.171	0.185
Estimated channel volume (cm^3)	714	825	892
Equivalent displaced Al mass (kg)	1.94	2.24	2.43
Manufacturing consideration	Continuous curved channel	Branched passages and junctions	Repeated circumferential passages and manifold connections

Note: The channel volume was estimated from the channel cross-sectional area, cross-sectional perimeter, and total heat-transfer area according to $V = A_{ch}S_{ht}/P_{wet}$.

4.2. Fluid–Thermal Coupled Analysis of the Traction Motor

4.2.1. Equivalent Models and Heat Transfer Coefficients of Motor Components

Heat transfer within the motor is primarily achieved through conduction and convection [28,29]. Thermal conduction primarily occurs between solid components in direct contact, such as the stator core and the windings, whereas thermal convection occurs between solid surfaces and the cooling fluid through fluid flow. The heat transfer mechanisms of the motor components are illustrated in Figure 3. The material specifications and thermophysical properties assigned to the principal components in the fluid–thermal model are summarized in Table 4.

During motor operation, the heat generated by different loss components is transferred through multiple thermal paths. The winding copper loss is initially transferred from the winding conductors to the surrounding insulation layer and the stator core via thermal conduction. Subsequently, heat is conducted from the stator core to the motor housing and finally removed by the coolant flowing through the cooling channels via convective heat transfer.

The iron losses generated in the stator and rotor cores are directly transferred through the corresponding solid regions, while the permanent-magnet eddy-current loss is mainly conducted from the magnets to the rotor core and adjacent components. In addition, heat transfer between the rotor and stator regions is influenced by the air gap, where heat exchange is relatively limited due to the low thermal conductivity of air. Therefore, the cooling-channel design mainly affects the heat dissipation capability by enhancing convective heat transfer at the motor housing–coolant interface.

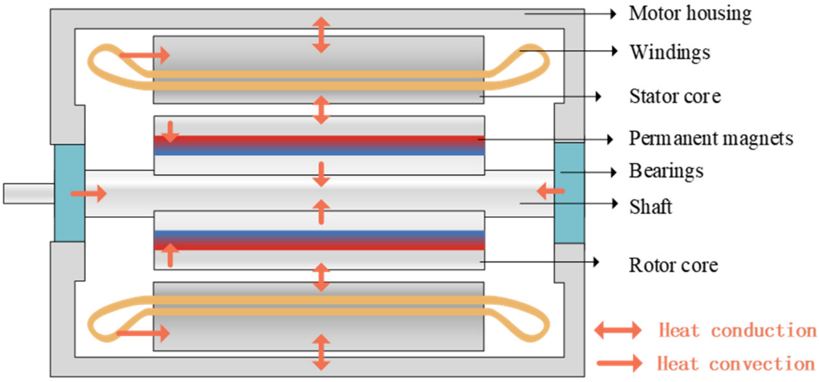

Figure 3. Heat transfer mechanisms of various motor components.

Table 4. Material specifications and thermophysical properties of the major motor components.

Component	Material	Density (kg/m^3)	Specific Heat Capacity (J/(kg·K))	Thermal Conductivity (W/(m·K))
Motor housing	Aluminum	2719	871	202.4
Iron core	Silicon steel	7800	446	40/40/1.2
Equivalent insulation layer	Composite	1900	1300	0.23
Equivalent winding	Copper	8500	380	387
Permanent magnet	NdFeB	7600	457	8.96
Air gap fluid	Air	1.225	1006.43	0.0242
Coolant	Water	998.2	4182	0.6

Liquid water was used as the coolant, and its thermophysical properties were treated as temperature-independent constants in the present simulations.

To reduce the complexity of mesh generation and improve computational efficiency while maintaining simulation accuracy [30,31], the following assumptions were adopted in the numerical model:

1. The thermal contact gaps between the stator and the housing, as well as between the windings and the stator slots, were neglected.
2. The power losses generated in the stator, rotor, windings, and permanent magnets were assumed to be uniformly distributed within each component.
3. The coolant was assumed to be an incompressible fluid, and the effect of gravity on the coolant flow was neglected.
4. Only heat conduction between motor components and convective heat transfer at the component surfaces were considered, whereas thermal radiation was neglected.
5. The influence of the skin effect in the windings on the loss distribution was neglected.
6. The outer surface of the motor housing was specified as a convective boundary with a uniform heat transfer coefficient.

Based on the above assumptions, a three-dimensional fluid–thermal coupled finite element model of the traction motor was established. The motor losses obtained from the transient electromagnetic finite element analysis were introduced as heat sources to calculate the temperature distribution and coolant flow characteristics. The corresponding computational mesh is shown in Figure 4.

The computational mesh was generated using polyhedral elements. Considering the complex geometry of the cooling channels and the strong thermal-fluid interactions at the interfaces between different materials, local mesh refinement was applied in these critical regions. The final computational domain contained approximately 9.39 million volume elements. The mesh quality was checked before the simulation to ensure sufficient numerical accuracy and convergence. The generated mesh provided adequate resolution to capture the coolant flow characteristics and temperature distribution within the traction motor.

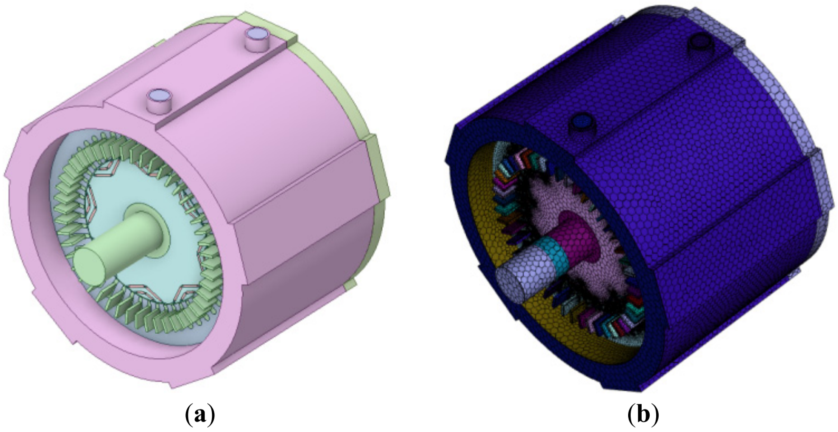

Figure 4. 3D model and mesh generation of the traction motor. (**a**) 3D model; (**b**) Meshed model.

4.2.2. Effect of Different Cooling Channel Configurations on the Motor Temperature Rise

Different cooling channel configurations have a significant influence on the heat dissipation performance of the motor [16]. To ensure a consistent comparison, the three cooling channel configurations were evaluated under the rated operating condition using the same coolant inlet temperature and total volumetric flow rate. The coolant inlet temperature was set to 40 °C, and the total volumetric flow rate was fixed at 10 L/min for each configuration. Since all three configurations employ the same circular inlet diameter of 25 mm, the corresponding average inlet velocity can be calculated as:

$$v = \frac{Q}{A} = \frac{4Q}{\pi D^2} = 0.340 \text{ m/s} \tag{7}$$

Therefore, an inlet velocity of 0.34 m/s was specified in the numerical model. Thus, the three cooling channel configurations were compared on an equal-total-flow-rate basis.

In addition to the inlet conditions, the outlet of the cooling channel was defined as a pressure outlet. The maximum inlet-outlet pressure difference was extracted from the static pressure distribution to characterize the hydraulic performance of different cooling-channel configurations. The interfaces between the coolant and solid components were treated as coupled interfaces to realize conjugate heat transfer. The calculated losses of the stator core, rotor core, windings, and permanent magnets were applied as volumetric heat sources in the corresponding regions. The external surface of the motor housing was defined with a convective boundary condition.

Because the contour plots in Figure 5 employ independently scaled color bars, the thermal performance of the three configurations is compared quantitatively using the maximum temperature values rather than the contour colors. As shown in Figure 5b, the highest temperature of the motor is mainly concentrated at the winding end region. The maximum temperatures are 98.2 °C, 97.2 °C, and 99.6 °C for the spiral, tree-shaped, and circumferential cooling channel configurations, respectively. This is mainly attributed to the high copper loss of the windings, where the generated heat is conducted through the stator core to the motor housing and is subsequently removed by the circulating coolant.

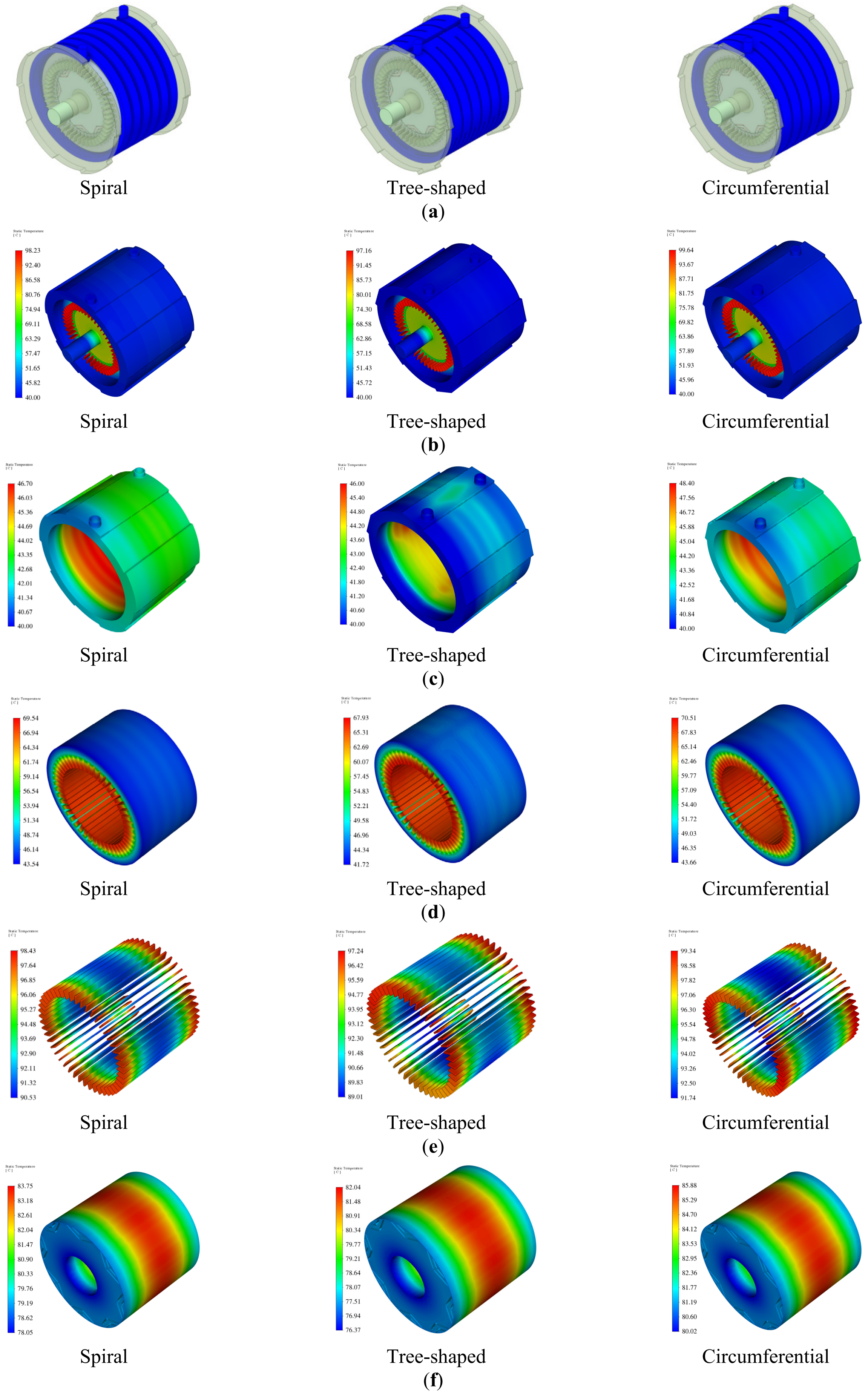
Spiral
Tree-shaped
Circumferential
(a)
98.23 92.40 86.58 80.76 74.94 69.11 63.29 57.47 51.65 45.82 40.00
Spiral
97.16 91.45 85.73 80.01 74.30 68.58 62.86 57.15 51.43 45.72 40.00
Tree-shaped
99.64 93.67 87.71 81.75 75.78 69.82 63.86 57.89 51.93 45.96 40.00
Circumferential
(b)
46.70 46.03 45.36 44.69 44.02 43.35 42.68 42.01 41.34 40.67 40.00
Spiral
46.00 45.40 44.80 44.20 43.60 43.00 42.40 41.80 41.20 40.60 40.00
Tree-shaped
48.40 47.56 46.72 45.88 45.04 44.20 43.36 42.52 41.68 40.84 40.00
Circumferential
(c)
69.54 66.94 64.34 61.74 59.14 56.54 53.94 51.34 48.74 46.14 43.54
Spiral
67.93 65.31 62.69 60.07 57.45 54.83 52.21 49.58 46.96 44.34 41.72
Tree-shaped
70.51 67.83 65.14 62.46 59.77 57.09 54.40 51.72 49.03 46.35 43.66
Circumferential
(d)
98.43 97.64 96.85 96.06 95.27 94.48 93.69 92.90 92.11 91.32 90.53
Spiral
97.24 96.42 95.59 94.77 93.95 93.12 92.30 91.48 90.66 89.83 89.01
Tree-shaped
99.34 98.58 97.82 97.06 96.30 95.54 94.78 94.02 93.26 92.50 91.74
Circumferential
(e)
83.75 83.18 82.61 82.04 81.47 80.90 80.33 79.76 79.19 78.62 78.05
Spiral
82.04 81.48 80.91 80.34 79.77 79.21 78.64 78.07 77.51 76.94 76.37
Tree-shaped
85.88 85.29 84.70 84.12 83.53 82.95 82.36 81.77 81.19 80.60 80.02
Circumferential
(f)

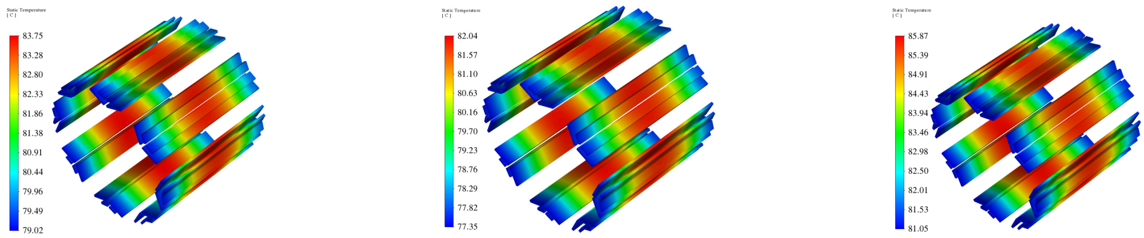

Spiral Tree-shaped Circumferential

(g)

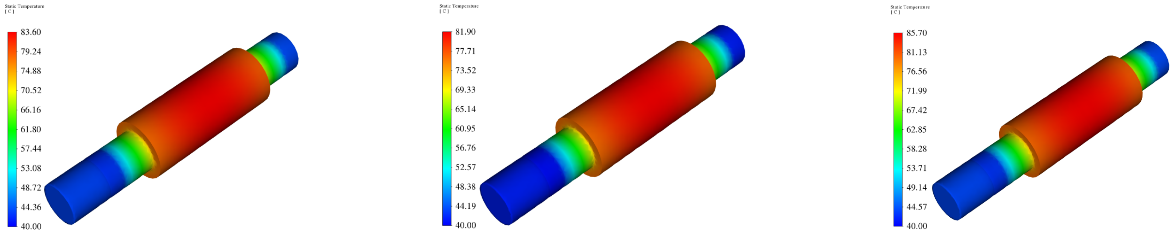

Spiral Tree-shaped Circumferential

(h)

Figure 5. Temperature distributions of the overall motor and various components under different cooling-channel configurations. The color bars of the individual contour plots are independently scaled; therefore, the contours are primarily used to illustrate the spatial temperature distribution and locations of hot spots. Quantitative comparisons among the three configurations are based on the reported maximum temperatures and Figure 6. (**a**) Motor model; (**b**) Temperature contours of the overall motor; (**c**) Temperature contours of the motor housing; (**d**) Temperature contours of the stator; (**e**) Temperature contours of the windings; (**f**) Temperature contours of the rotor; (**g**) Temperature contours of the permanent magnets; (**h**) Temperature contours of the shaft.

Although the three configurations have different heat-transfer areas and channel volumes, the thermal results do not exhibit a monotonic relationship with either parameter. For example, the circumferential channel has the largest total heat-transfer area (0.185 m^2) and the largest estimated channel volume (approximately 892 cm^3), but its maximum motor temperature reaches 99.6 °C. In contrast, the tree-shaped channel has a smaller heat-transfer area (0.171 m^2) and channel volume (approximately 825 cm^3), while achieving the lowest maximum motor temperature of 97.2 °C. This comparison indicates that the cooling performance cannot be attributed solely to the heat-transfer area or channel volume. The coolant-flow distribution and flow-path arrangement also have an important influence on the heat-removal capability.

The temperature distribution of the motor housing is presented in Figure 5c. The maximum housing temperatures are 46.7 °C, 46.0 °C, and 48.4 °C for the spiral, tree-shaped, and circumferential cooling channel configurations, respectively. Compared with other motor components, the motor housing exhibits the lowest temperature because the coolant continuously flows through the cooling channels integrated into the housing, thereby effectively removing heat from the housing surface.

The temperature distribution of the stator is shown in Figure 5d. The maximum stator temperatures are 69.5 °C, 67.9 °C, and 70.5 °C for the spiral, tree-shaped, and circumferential cooling channel configurations, respectively. The highest temperature is located in the stator slot region because the winding copper losses generate a large amount of heat, which is conducted to the stator core through the contact interface between the windings and the stator slots.

The temperature distributions of the windings are presented in Figure 5e. The maximum winding temperatures are 98.4 °C, 97.2 °C, and 99.3 °C for the three cooling channel configurations, respectively. Since the middle section of the windings is in close contact with the stator slots, most of the generated heat is transferred to the stator through thermal conduction, then conducted to the motor housing, and finally removed by the circulating coolant. In contrast, the winding end regions mainly dissipate heat through natural convection with the air inside the motor, resulting in a relatively lower heat transfer capability and consequently higher temperatures at the winding ends.

The temperature distributions of the rotor, permanent magnets, and shaft are shown in Figure 5f–h. Owing to the close thermal contact among these components, heat is transferred by thermal conduction, leading to relatively high and similar temperature distributions.

A comparison of the maximum temperatures of the motor components indicates that the circumferential cooling channel configuration exhibits the highest temperatures, followed by the spiral configuration, whereas the tree-shaped configuration achieves the lowest maximum temperatures, demonstrating the best cooling performance. The maximum temperatures of the motor components for the three cooling channel configurations are presented in Figure 6.

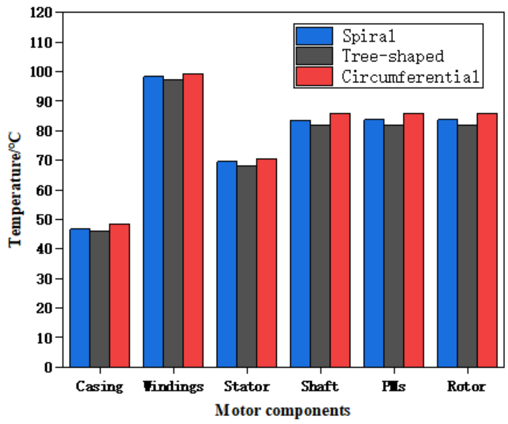

Figure 6. Comparison of maximum temperatures of various motor components for different cooling channel configurations.

4.3. Fluid Flow Analysis of the Traction Motor Based on Fluid–Thermal Coupling

4.3.1. Comparison of Static Gauge-Pressure Distributions and Maximum Inlet-to-Outlet Static-Pressure Differences

In the design of a traction-motor cooling system, both cooling performance and hydraulic characteristics should be considered, as emphasized in previous cooling-system studies [16,32]. In the present study, the maximum inlet-to-outlet static gauge-pressure difference is defined as the difference between the maximum static gauge pressure in the inlet region and the minimum static gauge pressure in the outlet region. This descriptive metric is used to characterize the extreme variation in the static-pressure field and to compare the three cooling-channel configurations under the same total coolant flow rate. A smaller value indicates a smaller extreme static-pressure variation according to the definition adopted in this study. However, this metric differs from the conventional pressure drop calculated using the area-weighted average of the inlet and outlet pressures and should not be interpreted as a total pressure loss. Therefore, it is not used to directly evaluate pumping power or cooling-system energy consumption in the present study. The cooling performance and the defined static-pressure-difference metric are consequently discussed as two separate aspects of cooling-channel performance.

Figure 7 presents the static gauge-pressure distributions of the coolant in the three cooling-channel configurations. Because the plotted pressure is referenced to the operating pressure adopted in the numerical model, local regions below this reference may exhibit negative gauge-pressure values. Based on the maximum static gauge pressure in the inlet region and the minimum value in the outlet region, the maximum inlet-to-outlet static gauge-pressure differences are 2096.4 Pa, 1816.3 Pa, and 2079.7 Pa for the spiral, tree-shaped, and circumferential cooling channels, respectively.

Under the same total coolant flow rate, the tree-shaped cooling channel exhibits the smallest maximum inlet-to-outlet static gauge-pressure difference among the three configurations, indicating a relatively small extreme variation in the static-pressure field according to the metric defined in this study.

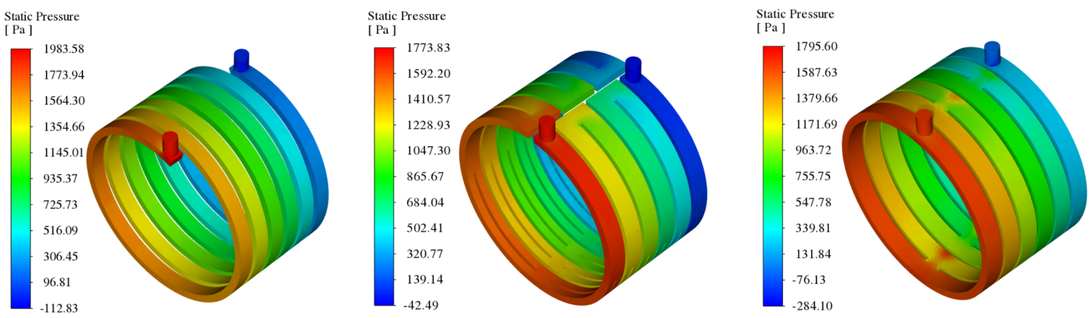

(**a**) (**b**) (**c**)

Figure 7. Static gauge-pressure contours of the three cooling-channel configurations. (**a**) Spiral; (**b**) Tree-shaped; (**c**) Circumferential.

4.3.2. Comparison of Coolant Velocity Distributions under Different Cooling Channel Configurations

The coolant velocity distributions for the three cooling channel configurations are shown in Figure 8. The spiral cooling channel exhibits a relatively uniform coolant flow, with a maximum velocity of 0.83 m/s and an average velocity of 0.53 m/s. The highest velocities are mainly observed near the coolant inlet and outlet. For the tree-shaped cooling channel, the maximum and average coolant velocities are 0.68 m/s and 0.34 m/s, respectively. The peak velocity occurs primarily at the channel bifurcations and turning regions, while relatively high velocities are also observed near the outlet. The circumferential cooling channel exhibits a maximum velocity of 0.91 m/s and an average velocity of 0.32 m/s, with the highest velocities mainly concentrated at the channel bends and the coolant outlet.

Overall, the spiral cooling channel provides the highest average coolant velocity, indicating a more uniform coolant flow throughout the channel. Although the tree-shaped configuration exhibits a relatively lower average velocity, its flow distribution is more balanced, which is beneficial for improving the uniformity of heat dissipation. In contrast, the circumferential cooling channel exhibits relatively high local velocities but a less uniform flow distribution, which may lead to localized flow concentration.

Therefore, a higher local coolant velocity does not necessarily guarantee better cooling performance, because the overall thermal performance depends on the magnitude and spatial distribution of the coolant velocity as well as the associated static-pressure characteristics.

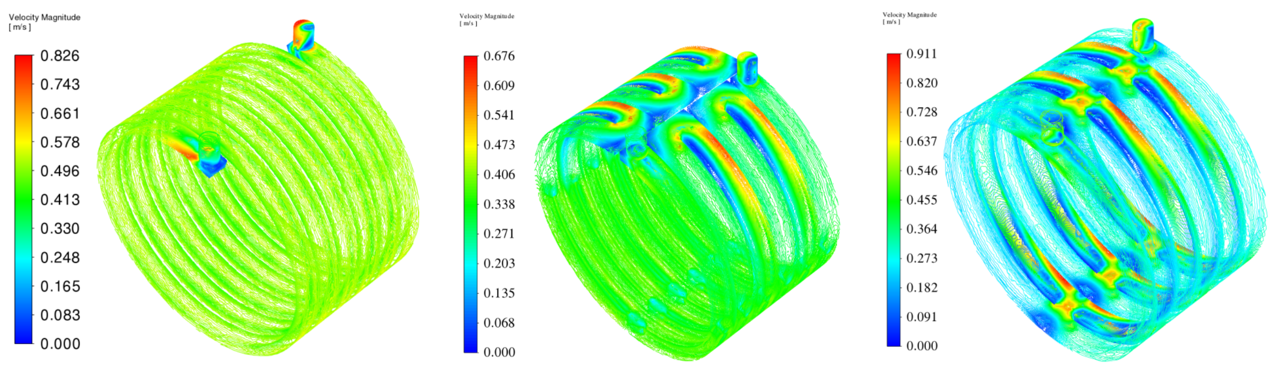

(**a**) (**b**) (**c**)

Figure 8. Coolant velocity contours under different cooling channel configurations. (**a**) Spiral; (**b**) Tree-shaped; (**c**) Circumferential.

Based on the coupled fluid-thermal analysis results, the three cooling-channel configurations exhibit different thermal, coolant-flow, and static-pressure characteristics. The tree-shaped cooling channel achieves the lowest maximum motor temperature and the smallest maximum inlet-to-outlet static gauge-pressure difference under the investigated condition. The spiral configuration provides intermediate thermal performance, whereas the circumferential configuration exhibits the highest component temperatures.

Based on the combined temperature results and the defined static-pressure-difference metric, the tree-shaped cooling channel is selected for the subsequent coolant-flow-rate analysis.

5. Coolant Flow Rate Matching for the Traction Motor under Different Working Conditions

5.1. Coolant Flow Rate Matching Under Peak Speed Working Conditions

The coolant flow rate significantly influences heat transfer between the coolant and the motor housing and also affects the maximum inlet-to-outlet static gauge-pressure difference. Therefore, the coolant flow rate should be selected by considering the thermal requirements together with the variation in this pressure metric.

Under the peak-speed operating condition, coolant flow rates ranging from 6 to 20 L/min are investigated. The maximum component temperatures obtained at the different flow rates are shown in Figure 9a, while Figure 9b presents the corresponding maximum inlet-to-outlet static gauge-pressure differences. As the coolant flow rate increases, the maximum motor temperature gradually decreases. However, once the flow rate reaches 12 L/min, the additional temperature reduction becomes relatively small.

Meanwhile, the maximum inlet-to-outlet static gauge-pressure difference increases with coolant flow rate. Considering the diminishing temperature-reduction benefit and the increase in the defined static-pressure-difference metric, 12 L/min is selected as the recommended design coolant flow rate under the peak-speed operating condition. This selection should not be interpreted as an optimization based on total-pressure loss or pumping power.

Particular attention should be paid to the thermal condition of the permanent magnets under peak-speed operation. The permanent magnets employed in the present motor are specified as N35UH-grade NdFeB magnets. This grade has a high intrinsic coercivity and a recommended maximum operating temperature of approximately 180 °C. Over the investigated peak-speed coolant-flow range, the maximum permanent-magnet temperature is approximately 129 °C, corresponding to a thermal margin of approximately 51 °C relative to the recommended maximum operating temperature. Therefore, the predicted magnet temperature remains below the recommended operating-temperature limit under the investigated cooling conditions. It should be emphasized, however, that this temperature margin does not constitute a complete verification against irreversible demagnetization, because demagnetization also depends on the temperature-dependent demagnetization curve, magnetic operating point, armature-reaction field, and field-weakening condition. Accordingly, the present comparison is interpreted as a thermal design margin for the permanent magnets.

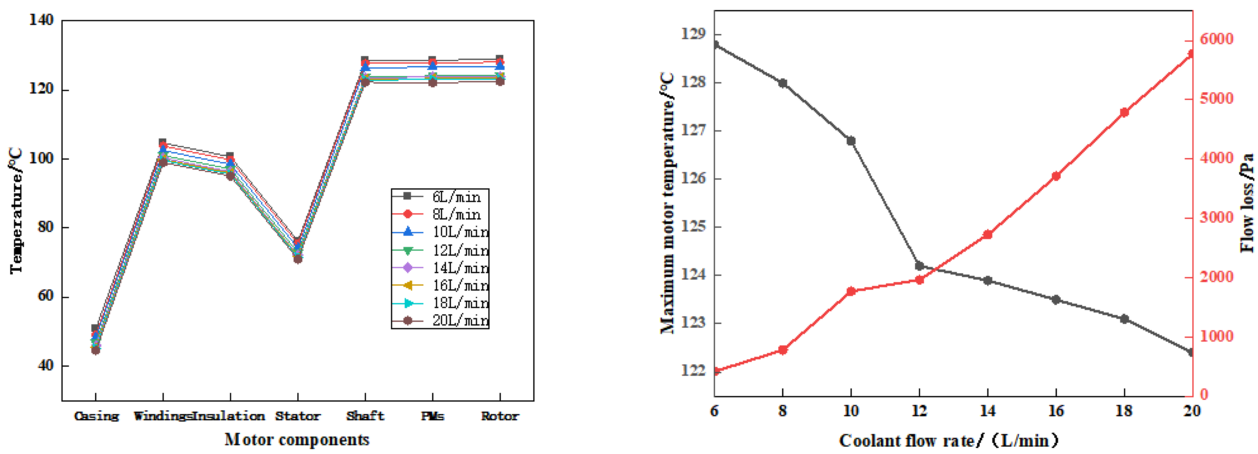

(**a**) Comparison of temperatures of various motor components under different coolant flow rates

(**b**) Variations of the maximum motor temperature and flow loss with respect to the coolant flow rate

Figure 9. (**a**) Maximum component temperatures and (**b**) maximum inlet-to-outlet static gauge-pressure difference under different coolant flow rates at the peak-speed operating condition.

5.2. Coolant Flow Rate Matching Under Peak Torque Working Conditions

Among the materials used in traction motors, electrical insulation materials are particularly sensitive to elevated temperatures [33]. Excessive thermal stress can accelerate insulation ageing and reduce the electrical reliability of the motor. Therefore, the temperatures of the winding and insulation system should be maintained within their respective allowable limits.

The thermal classification of the insulation system is referenced to IEC 60085:2007, while IEC 60349-4:2012 is used as an application-related reference for converter-fed permanent-magnet synchronous traction machines [34,35]. The motor investigated in this study employs a Class B insulation system, corresponding to thermal class 130. The maximum-temperature limits, winding temperature-rise limits, and performance reference temperatures for motors with different insulation classes are summarized in Table 5.

It should be noted that the absolute-temperature limit and the temperature-rise limit are two different physical quantities. For the Class B insulation system adopted in this study, the absolute-temperature limit of the insulation system is 130 °C, whereas the allowable winding temperature-rise limit is 80 °C. The temperatures obtained from the fluid–thermal simulations are absolute temperatures. When evaluating the winding temperature rise, the coolant inlet temperature of 40 °C is used as the reference temperature. Therefore, a 80 °C winding temperature-rise limit corresponds to an equivalent absolute winding-temperature limit of 120 °C.

Accordingly, two thermal safety criteria are applied in the subsequent peak-torque analysis: the absolute temperature of the insulation system should not exceed 130 °C, and the absolute temperature of the winding should not exceed 120 °C, where the latter corresponds to an 80 °C temperature rise relative to the 40 °C coolant inlet temperature.

Table 5. Temperature rise limits for motors under different insulation grades.

Insulation Class	A	E	B	F	H
Maximum temperature limit/°C	105	120	130	155	180
Winding temperature rise limit/°C	60	75	80	100	125
Performance reference temperature/°C	80	95	100	120	145

Note: The motor investigated in this study employs a Class B insulation system. With the coolant inlet temperature of 40 °C taken as the reference temperature, the allowable winding temperature rise of 80 °C corresponds to an equivalent absolute winding-temperature limit of 120 °C.

Under the peak-torque operating condition, coolant flow rates ranging from 8 to 24 L/min are selected, and the maximum temperatures of various motor components with respect to the flow rate are illustrated in Figure 10. At certain flow rates, the maximum temperatures of the motor windings and the insulation layer exceed the temperature limits of the Class B insulation system. Therefore, the selected design coolant flow rate must first satisfy the temperature constraints of the insulation system.

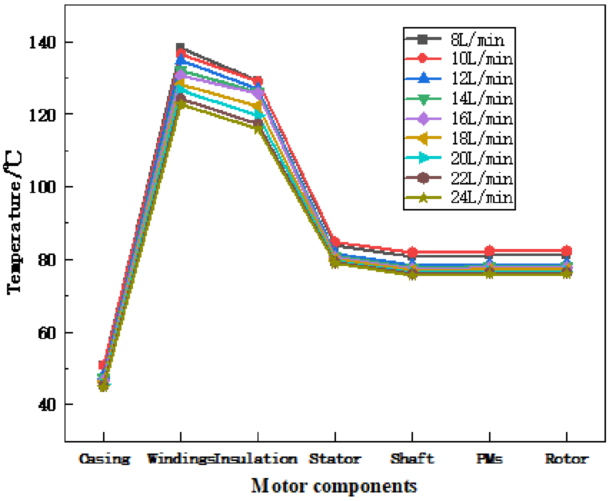

Figure 10. Maximum temperatures of various motor components under peak torque working conditions.

The variations in the maximum temperatures of the windings and insulation layer with coolant flow rate under the peak-torque operating condition are shown in Figure 11a. When the coolant flow rate reaches 12 L/min, the insulation-layer temperature falls below its allowable limit. As the flow rate is further increased in increments of 2 L/min, the winding temperature also satisfies its corresponding thermal safety criterion at 22 L/min. Figure 11b shows that the maximum inlet-to-outlet static gauge-pressure difference increases with coolant flow rate. Therefore, 22 L/min is identified as the minimum investigated coolant flow rate that satisfies both thermal constraints under the peak-torque operating condition, while the accompanying increase in the defined static-pressure-difference metric is also reported.

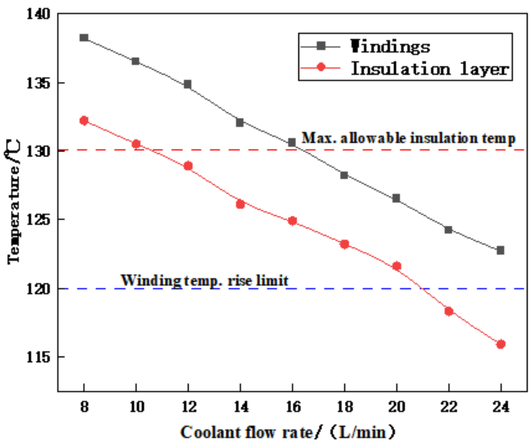

(**a**) Variation trends of the maximum temperatures of the windings and the insulation layer

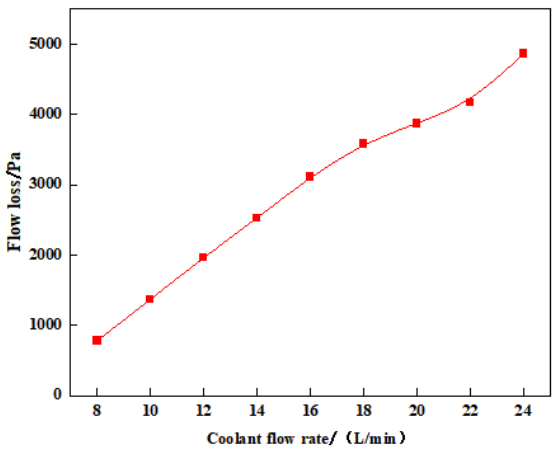

(**b**) Variation trend of the flow loss within the cooling channels

Figure 11. (**a**) Maximum winding and insulation-layer temperatures and (**b**) maximum inlet-to-outlet static gauge-pressure difference under different coolant flow rates at the peak-torque operating condition.

6. Conclusions

In this study, three cooling channel configurations for a dual-V permanent magnet synchronous motor were investigated based on fluid–thermal coupled analysis. The main conclusions are summarized as follows:

(1) The winding region exhibits the highest temperature due to the concentrated copper loss, making it the critical area for motor thermal management. Among the three cooling structures, the tree-shaped cooling channel achieves the best overall thermal performance, with the lowest winding, stator, and housing temperatures.

(2) Compared with the spiral and circumferential configurations, the tree-shaped cooling channel achieves lower component temperatures, a more balanced coolant distribution, and the smallest maximum inlet-to-outlet static gauge pressure difference at the same total coolant flow rate. This pressure metric represents the maximum static-pressure variation, not the total-pressure loss or the pumping power.

(3) The influence of coolant flow rate on motor temperature and the defined static-pressure-difference metric was further analyzed. A recommended design flow rate of 12 L/min was selected for the peak-speed operating condition based on the diminishing temperature-reduction benefit and increasing static-pressure difference.

Future research will further investigate the cooling performance under more complex operating conditions, including variable-speed operation, transient load variations, and multi-physics coupling effects involving electromagnetic, thermal, and fluid fields. In addition, optimization methods will be explored to achieve a better balance between cooling efficiency and hydraulic performance.

Nomenclature

Roman Symbols

Symbol	**Definition**
A	Cross-sectional area of the coolant inlet
A_{ch}	Cross-sectional area of the cooling channel
C_p	Specific heat capacity at constant pressure
$C_{p,s}$	Specific heat capacity of the solid material
D	Coolant inlet diameter
p	Pressure
P	Power loss of the corresponding motor component
P_{Σ}	Total power loss
P_c	Stator winding copper loss
P_{t1}	Rotor iron loss
P_{t2}	Stator iron loss
P_w	Permanent-magnet eddy-current loss
P_{Δ}	Sum of mechanical loss and stray loss
P_{wet}	Wetted perimeter of the cooling channel
q	Volumetric heat-generation rate
q_v	Volumetric heat-generation rate in the solid region
Q	Volumetric coolant flow rate
S_{ht}	Total heat-transfer area of the cooling channel
S_{vx},S_{vy},S_{vz}	Generalized source terms in the x-, y-, and z-momentum equations
S_T	Source term in the energy equation
t	Time
T	Temperature
u	Fluid velocity vector
v	Average coolant inlet velocity
v_x,v_y,v_z	Velocity components in the x-, y-, and z-directions
V	Volume
x,y,z	Cartesian coordinates

Greek Symbols

Symbol	**Definition**
ρ	Fluid density
ρ_s	Density of the solid material
μ	Dynamic viscosity
λ	Thermal conductivity of the fluid
λ_s	Thermal conductivity of the solid material
θ_1	First V-angle of the permanent-magnet arrangement

θ_2	Second V-angle of the permanent-magnet arrangement
Σ	Total or summation designation
Δ	Mechanical- and stray-loss designation

Subscripts

Subscript	**Definition**
x,y,z	Cartesian coordinate directions
s	Solid material
p	Constant-pressure condition
c	Stator winding copper loss
t_1	Rotor iron loss
t_2	Stator iron loss
w	Permanent-magnet eddy-current loss
v	Volumetric quantity
T	Energy-equation source term
ch	Cooling channel
ht	Heat-transfer area
wet	Wetted perimeter
Σ	Total power loss
Δ	Mechanical loss and stray loss
1,2	First and second V-angle quantities

Superscripts

Superscript	**Definition**
-	No superscript with a distinct physical meaning is used in the present formulation

Acronyms and Abbreviations

Acronym	**Definition**
CAD	Computer-aided design
CFD	Computational fluid dynamics
CHT	Conjugate heat transfer
ETN	Equivalent thermal network
FDM	Finite difference method
FEM	Finite element method
IEC	International Electrotechnical Commission
IPMSM	Interior permanent magnet synchronous motor
NdFeB	Neodymium–iron–boron
NEV	New energy vehicle
PM	Permanent magnet
PMSM	Permanent magnet synchronous motor
3D	Three-dimensional

Statement of the Use of Generative AI and AI-Assisted Technologies in the Writing Process

During the preparation of this manuscript, the authors used ChatGPT to assist with English-language editing and to improve the clarity and readability of the manuscript. After using these tools, the authors reviewed and edited the content as needed and take full responsibility for the content of the published article.

Author Contributions

Conceptualization, G.L., C.-Y.R. and Z.-L.L.; Methodology, G.L.; Software, Z.-L.L.; Validation, C.-Y.R.; Formal Analysis, C.-Y.R.; Investigation, W.Y. and Z.-L.C.; Writing, C.-Y.R.; Funding Acquisition, G.L.

Ethics Statement

Not applicable.

Informed Consent Statement

Not applicable.

Data Availability Statement

Data is available on request.

Funding

This work was supported in part by the National Key R&D Program of China under Grant 2023YFB4301500, and in part by the National Natural Science Foundation of China under Grant 52577034.

Declaration of Competing Interest

The authors declare that they have no known competing financial interests or personal relationships that could have appeared to influence the work reported in this paper.

References

1. Wang L, Wang X, Gao P, Liu S. Torque ripple reduction analysis of interior permanent magnet synchronous motor for electric vehicle. *Trans. China Electrotech. Soc.* **2024**, *39*, 6386–6396. DOI:10.19595/j.cnki.1000-6753.tces.231345
2. Kim KS, Lee BH, Kim HJ, Hong JP, Jun JH. Thermal analysis of outer rotor type IPMSM using thermal equivalent circuit. In Proceedings of the International Conference on Electrical Machines and Systems, Sapporo, Japan, 21–24 October 2012; pp. 1–4.
3. Kong X, Wang F, Xing J. Losses calculation and temperature field analysis of high-speed permanent magnet machines. *Trans. China Electrotech. Soc.* **2012**, *27*, 166–173. Available online: https://dgjsxb.ces-transaction.com/EN/abstract/abstract1728.shtml (accessed on 21 September 2026).
4. Yoon MK, Jeon CS, Kauh SK. Efficiency increase of an induction motor by improving cooling performance. *IEEE Trans. Energy Convers.* **2002**, *17*, 1–6. DOI:10.1109/60.986430
5. Boglietti A, Cavagnino A, Staton D, Shanel M, Mueller M, Mejuto C. Evolution and modern approaches for thermal analysis of electrical machines. *IEEE Trans. Ind. Electron.* **2009**, *56*, 871–882. DOI:10.1109/TIE.2008.2011622
6. Wang Y, Lin Y. Equivalent model of temperature field and temperature field analysis of interior permanent magnet synchronous motor based on electromagnetic-thermal bidirectional coupling. *Trans. China Electrotech. Soc.* **2025**, *40*, 7127–7139. DOI:10.19595/j.cnki.1000-6753.tces.241947
7. Boglietti A, Cavagnino A, Lazzari M, Pastorelli MA. A simplified thermal model for variable-speed self-cooled industrial induction motor. *IEEE Trans. Ind. Appl.* **2003**, *39*, 945–952. DOI:10.1109/TIA.2003.814555
8. Lim CH, Airoldi G, Bumby JR, Dominy RG, Ingram GI, Mahkamov K, et al. Experimental and CFD investigation of a lumped parameter thermal model of a single-sided, slotted axial flux generator. *Int. J. Therm. Sci.* **2010**, *49*, 1732–1741. DOI:10.1016/j.ijthermalsci.2010.03.018
9. Ghahfarokhi PS, Kallaste A, Vaimann T, Rassolkin A, Belahcen A. Steady-state thermal model of a synchronous reluctance motor. In Proceedings of the 2018 IEEE 59th International Scientific Conference on Power and Electrical Engineering of Riga Technical University (RTUCON 2018), Riga, Latvia, 12–13 November 2018; pp. 1–5.
10. Wahsh S, Shazly J, Yassin A. Steady-state heat conduction problems of AFPMSM using 3D finite element. In Proceedings of the 2016 Eighteenth International Middle East Power Systems Conference (MEPCON 2016), Cairo, Egypt, 27–29 December 2016; pp. 949–953.
11. Zhou H, Wang X, Zhao W, Liu J, Xing Z, Peng Y. Rapid prediction of magnetic and temperature field based on hybrid subdomain method and finite-difference method for the interior permanent magnet synchronous motor. *IEEE Trans. Transp. Electrif.* **2024**, *10*, 6634–6651. DOI:10.1109/TTE.2023.3334253
12. Joo D, Cho JH, Woo K, Kim BT, Kim DK. Electromagnetic field and thermal linked analysis of interior permanent-magnet synchronous motor for agricultural electric vehicle. *IEEE Trans. Magn.* **2011**, *47*, 4242–4245. DOI:10.1109/TMAG.2011.2149504

13. Zhang K, Qi Y, Le B, Feng Z. Design and experimental study of water cooling system for external rotor permanent magnet synchronous motor. *IEEE Access* **2024**, *12*, 88034–88047. DOI:10.1109/ACCESS.2024.3418017
14. Ma Z, Bu Z, Cheng J. Research on water-cooling structure design of permanent magnet synchronous motor. *Equip. Manag. Maint.* **2025**, 22–24. DOI:10.16621/j.cnki.issn1001-0599.2025.05D.08
15. Wang Y, Wang K, Zhu C. Analysis of temperature field and water-cooling heat dissipation of in-wheel motor. *Intern. Combust. Engine Parts* **2024**, 1–4. DOI:10.3969/j.issn.1674-957X.2024.23.001
16. Wang X, Dai Y, Luo J. Waterway design and temperature field analysis of vehicle permanent magnet synchronous motor based on fluid-solid coupling. *Trans. China Electrotech. Soc.* **2019**, *34* (S1), 22–29. DOI:10.19595/j.cnki.1000-6753.tces.L80816
17. Liu C, Lan Y, Li Y. Magnetic-thermal coupling analysis and channel optimization design of permanent magnet synchronous motor. *Micromotors* **2025**, *58*, 51–61. DOI:10.15934/j.cnki.micromotors.2025.07.006
18. Tang Y, Sun S, Yu W, Hua W. Thermal analysis of water-cooling permanent magnet synchronous machine for port traction electric vehicle. *Electronics* **2023**, *12*, 734. DOI:10.3390/electronics12030734
19. Jeon K, Park M, Park J, Choi H, Lee KD, Lee JJ, et al. Analysis of cooling characteristics of permanent magnet synchronous motor with different water jacket design using electromagnetic–thermal fluid coupled analysis and design of experiment. *Machines* **2023**, *11*, 903. DOI:10.3390/machines11090903
20. Zhang Z, Song Q, Wang X, Zhao S, Shah S WA. Reynolds-number-based optimization of a liquid cooling system for the permanent magnet synchronous motor of an electric vehicle. *Case Stud. Therm. Eng.* **2024**, *60*, 104720. DOI:10.1016/j.csite.2024.104720
21. Zhang Z, Song Q, Ahmed B, Han Y. Fluid and thermal effects on the temperature-dependent power increase of an electric vehicle's permanent magnet synchronous motor using a compound water-cooling method. *Case Stud. Therm. Eng.* **2025**, *65*, 105543. DOI:10.1016/j.csite.2024.105543
22. Wan Y, Li Q, Guo J, Cui S. Thermal analysis of a Gramme-ring-winding high-speed permanent-magnet motor for pulsed alternator using CFD. *IET Electr. Power Appl.* **2020**, *14*, 2202–2211. DOI:10.1049/iet-epa.2020.0086
23. Versteeg HK, Malalasekera W. *An Introduction to Computational Fluid Dynamics: The Finite Volume Method*, 2nd ed.; Pearson Education Limited: Harlow, UK, 2007.
24. Ding S, Cui G, Li Z, Guan T. Fluid and thermal performance analysis of PMSM used for driving. *Heat Mass Transf.* **2016**, *52*, 571–579. DOI:10.1007/s00231-015-1581-8
25. Guo C, Long L, Wu Y, Xu K, Ye H. Electromagnetic-thermal coupling analysis of a permanent-magnet in-wheel motor with cooling channels in the deepened stator slots. *Case Stud. Therm. Eng.* **2022**, *35*, 102158. DOI:10.1016/j.csite.2022.102158
26. Feng L, Ning Y, Zhang H, Feng Y, Wang M. Double-layer counter-flow cooling structure design and analysis of outer-rotor permanent magnet synchronous motors. *Mach. Tool Hydraul.* **2026**, *54*, 162–168. DOI:10.3969/j.issn.1001-3881.2026.02.022
27. Hu Y, Li J, Jia J, Zhao S, Cao J, Song F, et al. Structural optimisation of cooling waterway for vehicle motors based on fluid-solid coupling. *Small Spec. Electr. Mach.* **2025**, *53*, 33–37. Available online: https://www.wdj21.com/ssemj/CN/abstract/abstract1435.shtml (accessed on 16 September 2026).
28. Liu L, Wang D, Chen D. Equivalent thermal network modeling and temperature field analysis of oil-cooled IPMSM. *J. Hubei Univ. Automot. Technol.* **2026**, *40*, 54–59. DOI:10.3969/j.issn.1008-5483.2026.01.010
29. Kang Y. Cooling structure design and temperature field analysis of electric vehicle drive motor. *Electron. Commun. Comput. Sci.* **2025**, *7*, 115–117. Available online: https://ojs.omniscient.sg/index.php/eccs/article/download/69593/68135/ (accessed on 16 September 2026).
30. Wu B, Wan Z, Zhang K, Xi R, He M. Design of reentrant cooling channel in permanent magnet synchronous motor considering temperature field and flow field. *Trans. China Electrotech. Soc.* **2019**, *34*, 2306–2314. DOI:10.19595/j.cnki.1000-6753.tces.171483
31. Peng DQ, Zeng H, Zhang ZK, Yin W, Yan CS, Li G, et al. Simulation of enhanced heat dissipation performance of large permanent magnet synchronous motor with internal and external double cycles. *J. Hunan Univ. (Nat. Sci.)* **2024**, *51*, 195–203. DOI:10.16339/j.cnki.hdxbzkb.2024239
32. Gai Y, Chong YC, Adam H, Deng X, Popescu M, Goss J. Thermal analysis of an oil-cooled shaft for a 30,000 r/min automotive traction motor. *IEEE Trans. Ind. Appl.* **2020**, *56*, 6053–6061. DOI:10.1109/TIA.2020.3025745
33. Xu Z, Xu Y, Gai Y, Liu W. Thermal management of drive motor for transportation: Analysis methods, key factors in thermal analysis, and cooling methods—A review. *IEEE Trans. Transp. Electrif.* **2023**, *9*, 4751–4774. DOI:10.1109/TTE.2023.3244907

34. *IEC 60349-4:2012*; Electric traction—Rotating Electrical Machines for Rail and Road Vehicles—Part 4: Permanent Magnet Synchronous Electrical Machines Connected to an Electronic Converter. International Electrotechnical Commission: Geneva, Switzerland, 2012.
35. *IEC 60085:2007*; Electrical Insulation—Thermal Evaluation and Designation. International Electrotechnical Commission: Geneva, Switzerland, 2007.